MOX-Report No. 49/2019

In silico model of the early effects of radiation therapy on the microcirculation and the surrounding tissues

Cicchetti, A.; Laurino, F.; Possenti, L.; Rancati, T.; Zunino, P.

MOX, Dipartimento di Matematica
Politecnico di Milano, Via Bonardi 9 - 20133 Milano (Italy)

mox-dmat@polimi.it http://mox.polimi.it

In silico model of the early effects of radiation therapy on the microcirculation and the surrounding tissues

Alessandro Cicchetti[1,*], Federica Laurino[2,*], Luca Possenti[1,3], Tiziana Rancati[1,"], and Paolo Zunino[2,"]

[1]Prostate Cancer Program, Fondazione IRCCS Istituto Nazionale dei Tumori di Milano, Milan, Italy
[2]Laboratory for Modeling and Scientific Computing MOX,Department of Mathematics, Politecnico di Milano, Milan, Italy
[3]LabS,CMIC Department, Politecnico di Milano, Milan, Italy
[*]Both authors contributed equally to this manuscript
["]Both authors contributed equally to this manuscript

corresponding author: Alessandro Cicchetti (alessandro.cicchetti@istitutotumori.mi.it)

keywords: simulations; microcirculation; computational model; radiation toxicity; microenvironment

nothing to disclosure

Abstract

Background: Radiation-induced organ dysfunction are frequently described by Normal Tissue Complication Probability models. The approximations of this radiobiological approach do not allow to consider the important role played by the microvasculature not only in the dose-response of the blood vessels, but also of the organs where it is located. To this purpose we presented a computational model of the damage induced by RT on the microcirculation and of its effects on the normal tissues surrounding the tumour. Material and Methods: The effects of the ionizing radiation on the capillary bed are mediated by the inflammatory response. We derived from a literature search the possible morphological and functional variations of the network due to the process of the acute inflammation. Specifically, we considered a vasodilation, an increased membrane permeability with a consequent fluid extravasation and an increasing in the wall elasticity. These perturbations to the system were included in a computational model, already able to describe the physics of the microcirculation and of its exchanges with the surrounding tissues. Results:Two computational descriptions were considered. In the first one, we changed a set of 4 parameters associated to the increased fluid exchange from the health scenario at the baseline to a seriously compromised scenario with the oedema formation. The second study investigated the effect of a perturbation to the vessel wall elasticity. Conclusions: These simulations represent a first step towards the challenging objective of understanding, and describing in a mechanistic way the effects of radiation on the vascular microenvironment.

1 Introduction

Dose-response curves for tumour and normal tissues were constructed for the first time in 1934 by Holthusen to describe skin cancer control and side-effects in the surrounding epidermial area. For both the outcomes the well-known sigmoid-shaped relationship was observed. The so-called Tumour Control Probability model and Normal Tissue Complication Probability model (TCP and NTCP, respectively) were the first tools used by radiobiologists and oncologists to determine the best radiotherapy (RT) dose prescription to the tumour. This optimal prescription results from a compromise. Indeed, the goal of radiotherapy is to deliver high doses of ionizing radiation (IR) to eradicate tumour cells, minimizing the risk of damaging the surrounding normal tissues. The consequent balance, or ratio, is known in literature as the therapeutic index and it should be optimized to give the best clinical outcome. On the other hand, at a preclinical level, the traditional radiobiological approach considers injury to individual cell lines modelled by cell culture. However, organised tissues and organs include a large number of interacting and mutually dependent cells [1]. Particularly, microvasculature endothelial cells (ECs) and smooth muscle cells play an important role not only in the dose-response of the blood vessels, but also of the organs where they are located. This evidence was already supported by the relative seriality NTCP model, in which the intrinsic serial behaviour of organs was mixed with the parallel architecture of microvasculature [2] to describe the dose-response relationship of a specific organ at risk. This happens because microcirculatory vessels (exchange vessels) are embedded within an organ while most macrocirculatory vessels (arterial resistance vessels and venous return vessels) are not. Radiation damage to arterioles, capillaries and venules, i.e. to the smallest and most sensitive structures of the cardiovascular system, have been largely investigated in animal studies during the 70s [3, 4, 5]. More recently, changes in the vascular function have been observed before the occurrence of late fibrosis and atrophy tissues in cancer patients [4, 6], supporting the idea that vascular damage acts in all late radiation injury. As a matter of fact, it is currently accepted that pathogenesis of chronic radiation effects is based on complex pathophysiological processes, which involve radiation-induced changes in organ-specific parenchymal cells (cell death), fibroblasts (differentiation) and vascular ECs (loss of capillaries). Such an orchestrated response results in progressive parenchymal damage and sometimes in loss of function within the irradiated volume.

In addition, several trials have found an increased risk of late normal tissue toxicity for patients with medical conditions or specific habits that adversely affect the stability of the vascular system (hypertension, diabetes, smoking, alcohol abuse, obesity, use of cholesterol-lowering drugs, use of drugs for cardiac morbidity) [7, 8, 9, 10, 11]. Indeed, the direct and indirect (the inflammatory response) effects of the reactive oxygen species on a capillary bed can induce impairments in the network which gets worse during the subsequent months reaching an irreversible level of damage that critically affects organ functionality [1, 4]. Such a phenomenon may also involve bigger vessels, even seriously

compromising the macrovasculature [12, 13].

As reported from the present state of understanding which is mainly based on animal models, radiation-induced cardiovascular diseases may occur in both the micro- and macro-vasculature. For instance with specific reference to the heart, at the microscale, capillary density is decreased, causing chronic ischemic heart disease and focal myocardial degeneration, whereas at the macroscale development of age-related atherosclerosis is accelerated in coronary arteries [14].

For all of these reasons, the understanding of how IR affects the vasculature in both the tumor microenvironment and in normal tissues is crucial. However, gathering more insight about these mechanisms is limited by the difficulty in visualizing the response of these interdependent components over time and in vivo. Statistical models (i.e. only based on the extensive collection of data and on the search for association between covariates and endpoint) are not suitable to describe this complexity within the microenvironment. To this purpose, we present here a computational model of the damage induced by RT on the microcirculation and of the effect of IR on normal tissues surrounding the tumour.

2 Materials and Methods

The functional units of the capillary beds were selected as the target of this study, considering (i) small arterioles, (ii) capillaries, and (iii) post-capillary venules. Such vessels differ in terms of geometry, components and physical characteristics. Since RT can affect all of these three aspects, the treatment may results in different outcome on the different vessels. In the following section, we introduce a computational model to account for the detrimental effect to the microcirculation due to irradiation and leveraging literature information on the radiation-induced variations of the biophysical parameters, which characterize the interaction of the vascular network with the surrounding tissue.

2.1 A Mathematical Model for Microcirculation

We extend the model derived in Possenti et al. [15] describing the blood flow in a microvascular network and the interstitial flow in the surrounding volume to take into account the deformation of the vessels due to the pressure load and to the increased permeability of the endothelium. The starting point is a fluid dynamic problem defined in a three-dimensional (3D) domain Ω, which is split into two subdomains representing the tissue and the vasculature. However, the full-3D description of the problem is inevitably associated with several technical difficulties related to the morphological complexity of the vasculature combined with the physical complexity of the blood flow. Moreover, we use computational methods to approximate the solutions of such models. As a consequence, the mathematical and computational complexity of the approach must also kept under control. Therefore, with the aim of developing a model able to handle also complex vascular networks with a reasonable computational cost, we apply

the model reduction technique based on averaging introduced in the literature [16, 17]. More precisely, we transform the initial 3D problem defined in the vasculature into a 1D problem defined on the central axis of the vessels (denoted with Λ in what follows). The interaction between the vasculature and the interstitial volume is described by means of an equivalent source term distributed on the physical interface of the vessel wall, called Γ. This approach mitigates the poor regularity of the 3D problem and guarantees, by consequence, more robust properties of the solution and of the numerical approximation, as shown in Laurino et al. [17].

Governing equations. For the tissue domain Ω we use standard Cartesian coordinates, denoted by $\mathbf{x}$. For the vascular domain Λ the arc-length s is introduced, which is a one-dimensional coordinate system along the branches of the vascular network. The unknown quantities of the problem are pressures $p_t(\mathbf{x})$, $p_v(s)$, hematocrit $H(s)$, and velocities $\mathbf{u}_t(\mathbf{x})$, and $u_v(s)$ ($\mathbf{u}_v = u_v = u_v\boldsymbol{\lambda}$, with $\boldsymbol{\lambda}$ the tangent unit vector at each point of the vascular network). Velocities and pressures for both the domains are determined by solving the following governing equations:

$$\mathbf{u}_t + \frac{k}{\mu}_t \nabla p_t = 0 \quad \text{in } \Omega \qquad \textit{Interstial flow} \qquad (1)$$

$$\nabla \cdot \mathbf{u}_t + L_p \frac{S}{V}_{LF} (p_t - p_L) - f(\overline{p}_t, p_v)\delta_\Gamma = 0 \quad \text{in } \Omega \qquad \textit{Mass balance} \qquad (2)$$

$$-\mu_v \rho_v u_v + |\Sigma| \frac{\partial p_v}{\partial s} = 0 \quad \text{on } \Lambda \qquad \textit{Blood flow} \qquad (3)$$

$$\frac{\partial \left(|\Sigma| u_v\right)}{\partial s} + |\gamma| f(\overline{p}_t, p_v) = 0 \quad \text{on } \Lambda \qquad \textit{Mass balance} \qquad (4)$$

We assume that the tissue Ω can be modeled as an isotropic porous medium. As a consequence, the Darcy's law (equation (1)) is used to describe the fluid permeation across the tissue, together with the mass balance equation (equation (2)). Here, $\overline{p}_t$ is the average pressure computed on the boundary of the vessel cross-section normal to the centerline Λ. In addition, we consider the lymphatic drainage because it is relevant in this context. Lymphatic system drains the excess of fluid from the interstitial space to the venous system. Such a drainage is taken into account in equation (2) by including a sink term which is defined by (i) the hydraulic conductivity of the lymphatic wall, denoted here by L_p^{LF}, (ii) the surface area of the lymphatic vessels per unit volume of tissue, $\frac{S}{V}_{LF}$, and (iii) the hydrostatic pressure difference between the interstitial space and the lymphatic vessels, p_L. Concerning the vasculature, equation (3) is the model for laminar flow in a straight channel, where Σ is the vessel cross-section and ρ_v is a parameter related to the hydraulic resistance which is modulated according to the area and the shape of the cross-section of each micro-vessel. It is important to note that the model provides a steady description of the flow. Such an assumption is reasonable in distal regions of a microvascular network in which

the pulsatility of the flow becomes negligible [18]. Equation (4) accounts for the fluid leakage from the vessel to the surrounding tissue. In particular, the term f describes the fluid flux across the vascular wall according to the classical Starling's model of filtration for semipermeable membranes [19]

$$f(\overline{p}_t, p_v) = L_p((p_v - \overline{p}_t) - \sigma(\pi_v - \overline{\pi}_t)), \tag{5}$$

where L_p denotes the hydraulic conductivity of the vessel and $p_v - \overline{p}_t$ is the pressure drop between the vasculature and the surrounding tissue. The effect of blood proteins on the pressure field is taken into account via an osmotic pressure jump across the membrane $\pi_v - \pi_t$, which is assumed constant in time and uniform in space, and the Staverman's osmotic reflection coefficient σ, which describes the molecular sieving property of the capillary wall. The presence of the red blood cells (RBC) is described through the hematocrit $H(s)$, computed using the following equation

$$|\Sigma| u_v \frac{\partial H}{\partial s} - |\gamma| f(\overline{p}_t, p_v) = 0 \quad \text{on } \Lambda. \quad \textit{Hematocrit}, \tag{6}$$

where and Σ is the cross section of the vessel normal to the centerline and γ is its boundary. Such equation prescribes a conservation principle for hematocrit, due to the inability of RCB to extravasate. Equation (6) is complemented by a model (i) to compute the blood apparent viscosity based on radius and hematocrit results and (ii) to consider the heterogeneous split of RBC when flowing through bifurcations (see Possenti et al. [15] and Supplementary Materials for more details).

Concerning the boundary conditions, we define the inflow and outflow sections of the vascular network Λ_{in} and Λ_{out}, respectively. Doing so, a pressure gradient along the blood vessels is imposed. For H, since only an inlet boundary condition is required, we enforce the value H_0 at the network inflows Λ_{in}. Lastly, we adopt mixed conditions for the interstitial domain Ω. Here, p_0 is a far field pressure value and β_t can be interpreted as an effective conductivity accounting for layers of tissue surrounding the considered sample. Such modelling choices translate into the following conditions:

$$p_v = p_{in} \quad \text{on } \Lambda_{in} \tag{7}$$

$$p_v = p_{out} \quad \text{on } \Lambda_{out} \tag{8}$$

$$H = H_{in} \quad \text{on } \Lambda_{in} \cap \partial\Omega \tag{9}$$

$$\mathbf{u}_t \cdot \mathbf{n} = -k_t \nabla p_t \cdot \mathbf{n} = \beta_t (p_t - p_0) \quad \text{on } \partial\Omega \tag{10}$$

2.2 A mathematical model for deformable microvessels

We analyze here the vessels with a mechanical point of view, following the approach adopted in Causin et al. [20]. The wall of a vessel consists in a single layer of endothelial cells, a basement membrane and a layer made of fibrils, like collagen. This last component makes the wall elastic and compliant to stresses. Hence, we represent the capillary wall as an elastic material characterized by

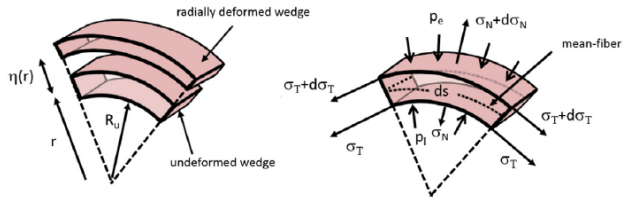

Figure 1: *Infinitesimal wedge-shaped radial section used for the derivation of the balance equations for ring model with circular cross-section. Left: radial deformation. Right: tangential stress σ_T, normal stress σ_N acting on the wedge faces. Figure from [20].*

a Young modulus and a Poisson's ratio. Arterioles are equipped also with one or two layers of smooth muscle cells. This feature makes the arterioles' wall much thicker compared to the venules', and therefore more resistant to pressure loads and not prone to collapse. Thus, we distinguish between the two, namely between thick-wall structure and thin-wall structure, according to the vessel wall thickness-to-radius ratio. Furthermore, venules may fall into buckling. If the pressure load becomes high enough, the wall firstly looses the starting circular cross-section turning into an elliptical shape. Then, the closest opposite sides of the section approach each other, until they touch forming a dumbbell-like shape. This behaviour is mathematically defined like in Tadjbakhsh et al. [21].

From a mathematical point of view, we describe the vessel cross-section area and shape as a function of the pressure loads. Combining a structural model of the micro-vessels with the flow equations described above, we build a mathematical model that represents the dependence of the hydraulic resistance of each micro-vessel on the transmural pressure $\Delta p = (\bar{\bar{p}}_t - p_v)$. In the structural model, each vessel is modelled as an elastic ring with a Young modulus E of an incompressible material ($\nu = 0.5$), assumed to be circular in the undeformed conditions characterized by radius R_u, thickness h_u. As said above, venules (thin-walled vessels) may assume a buckled configuration whereas such a behaviour is not commonly seen in arterioles (thick-walled vessels). Note that even a not completely closed vessel may result in a functional loss of the vessel within the network. As a matter of fact, it suffices the section to be small enough to prevent red blood cells passage to compromise its physiological function. For these reasons, we split the mechanical model for deformable microvessels into two parts, the pre-buckling regime and the post-buckling regime.

Pre-buckling regime On applying the internal and external pressure loads, radial and circumferential stresses arise in the ring. In the pre-buckling regime, we assume axisymmetry and plane stress conditions. Then, using the notation sketched in Figure 1 and applying the equilibrium condition between radial and

tangential stresses, namely

$$\frac{d\sigma_N}{dr} + \frac{1}{r}(\sigma_N - \sigma_T) = 0,$$

we obtain the following formulas for the deformed radius of the vessel:

$$R = R_u \left(1 + \frac{(1-\nu)}{E} B_1 - \frac{1+\nu}{E} \frac{B_2}{R_u^2}\right) \qquad \text{thick-walled ring} \qquad (11)$$

$$R = R_u \left(1 - \frac{1-\nu^2}{\gamma E} \Delta p\right) \qquad \text{thin-walled ring} \qquad (12)$$

where for thick vessels R denotes the internal radius and the coefficients B_1, B_2 depend on the nominal radius and thickness, R_u and h_u, and on the transmural pressure Δp, see Supplementary Materials for more details. The coefficient the hydrodynamic resistance ρ_v depends on the flow profile, the radius R and the curvature of the vessel (see Possenti et al[15]). In our cases, we consider straight cylindrical channels, namely no curvature is involved, and thus the flow is described by means of the standard Poiseuille parabolic flow profile. As a consequence, ρ_v is constant, precisely $\rho_v = -8$, and the deformed radius R plays a role in (3) only through the cross-section area $|\Sigma|$.

Post-buckling regime When considering buckled configurations, the model must also keep into account the bending actions which actually lead to the loss of axial symmetry. Furthermore, in this phase, the ring undergoes deformations in its shape, not in its length, hence only isoperimetric deformations are considered, see Figure 2. However, the complexity of the mathematical model is greatly increased due to the balance of bending moments and forces on the infinitesimal wedge-shaped radial section of ring. Indeed, this translates into differential equations that can not be solved explicitly. To deal with this complexity, we have set up a hybrid analytical/computational approach. The purpose of such an approach is to compute the hydrodynamic resistance of the deformed vessel in the post-buckling regime, i.e. ρ_v, given the undeformed vessel configuration R_u, h_u and the transmural pressure Δp. More precisely, the hydrodynamic resistance depends on the (normalized) flow profile in the cross-section, u_v^*, as follows:

$$\rho_v = -\frac{|\Sigma|^2}{R^4 \int_{\Sigma^*} u_v^* d\Sigma^*}. \qquad (13)$$

Using the post-buckling model, the shape of the cross-section of the vessel and the corresponding normalized flow profile u_v^* are determined numerically for any vessel such that the transmural pressure overcomes the buckling instability threshold.

Applying Pre- and Post- buckling regime Given R_u and h_u, we compute the thickness-to-radius ratio to distinguish the thick-walled structures (arterioles) from the thin-walled ones (capillaries and venules) and use equations (11)

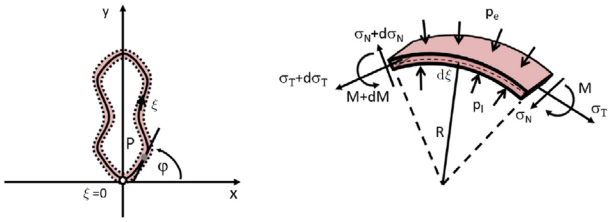

Figure 2: *Left: coordinate system for the thin-walled ring model in buckled configuration. Right: tangential stress σ_T, normal stress σ_N and bending moment M acting on the wedge faces. Figure from [20].*

and (12) to compute the deformed radius. For the latter, we can discriminate the pre- and the post-buckling regime on the basis of the Δp and compute the hydrodynamic resistance ρ_v when buckling occur as in equation (13).

2.3 The acute effect of RT on microcirculation and its impact on the model parameters

After irradiation within the therapeutic range, an early transient inflammatory response occurs in normal tissues. As a matter of fact, IR is an external physical agent that alters the biochemical balance in healthy tissues causing a reaction mediated by the inflammation. Thus, the biological pathway is basically as the one defined by Celsus [22] at the time of the ancient Romans: *calor (heat), rubor (redness), tumor (swelling), dolor (pain)* and, as already said, the *functio laesa (impaired function)* of the surrounding structure.

The pattern of response is different in vessels of different dimensions. This is presumably related to differences in the vessel geometry and the composition of their wall (elastin, collagen, fibroblasts and smooth muscle cells), which vary between the functional units of the cardiovascular system [4]. In particular, the capillary bed is the most sensitive region of the cardiovascular system. From a chronological point of view, it is also the first to be altered and, possibly, seriously compromised. The potential impairment of veins and arteries requires more time to show up.

However, the vascular damage is not easily separated into early (transient), intermediate and late (chronic) changes. There is evidence of a smooth gradual decrease in vascular functioning from minor alterations to major unequivocal changes during the development of late effects. Due to this consequentiality, the focus of this study is to describe the early changes in the microcirculation during the first hours after a single RT fraction, i.e. the morphological and functional variations. To this aim, we described the two main phases of the acute inflammation: the haemodynamic changes and the functional changes.

Haemodynamic changes The haemodynamic changes occur mainly in the arterioles. They are characterized by a first transient vasoconstriction (haemostasis) which can be ignored in this study since it appears for a few seconds right after irradiation. Subsequently, vasoconstriction is followed by a persistent and progressive vasodilation (by half an hour from IR injury). Such a dilation process may be promoted by histamine-like substances, which are released from dying epithelial cells [23]. As a consequence, blood volume in the microvascular bed of the irradiated area is increased and a consequent redness occur (erythema and warmth). Vasodilation mainly involves arterioles because at the capillary ends an adequate blood velocity must be guaranteed in order to favor the gas and nutrients exchanges with the extravascular space. Thus, progressive vasodilation elevates the local hydrostatic pressure. To describe the effect of such a variation, we have varied the prescribed hydrostatic pressure at the network inlet.

Functional changes The changes in the vascular membrane are caused by a direct and indirect effects of IR. To describe the direct effect on the vessel wall, we considered the findings of the in vitro study by Kabacik et al. [24]. They irradiated EC layer at 0.5, 2 and 10 Gy, showing that radiation exposure increases the permeability of the endothelial layer through the disruption of EC junctions, which are made up of the endothelial adhesion molecule cadherin. In addition, they proposed a mechanism of IR-induced endothelial permeability. Briefly, cells irradiation triggers the production of reactive oxygen species, which causes a rise in the concentration of intracellular calcium. This stimulates the activation of the "A Disintegrin and metalloproteinase domain-containing protein 10 " (ADAM10) which cleaves the cadherin, weakening cell junctions and increasing endothelial permeability. Moreover, by using macromolecules of different sizes, they showed how endothelium permeability depends on the dose, particularly for the larger macromolecules (i.e. higher kDa). Another direct effect of IR is the apoptosis or necrosis of muscle cells or ECs, which eventually increases the vascular permeability [4, 1].

On the other hand, the formerly described vasodilation also contributes as an indirect effect altering the membrane permeability. Indeed, the local hydrostatic pressure acts also on the fluid convective flow into the extracellular space. Thus, through the endothelial barrier, the vasculature slowly leaks plasma proteins, platelets, fibrin and circulating leukocytes (activated by inflammation) into the interstitium. IR also causes complex alteration of the vessel wall, which can be summarised as (i) the adhesion and infiltration of substances in the wall membrane, (ii) the partial sloughing or the swelling of the ECs (more evident in an intermediate phase, i.e., 2-6 months after the end of RT) and also in the compromised condition of the endothelial glycocalyx layer.

Summarizing, large increases of the hydraulic conductivity, reductions of the osmotic reflection coefficient (which describes the molecular sieving property of the capillary wall) and decrease of wall mechanical properties (i.e. the Young modulus E) occur during the first phase of acute inflammation. The magnitude

of the changes usually results in a short-lived effect [25]. However, a high dose level or a moderate dose in an already impaired system may have an impact on the reversibility of the process, consequently producing long-lasting effects.

Oedema and fibrin deposition The characteristic inflammatory oedema appears in the interstitial space because of the two radiation induced processes formerly described, which provide a double contribution in fluid escape by convective flow (hydrostatic pressure) and by exudation due to the membrane permeability. Sometimes, fibrin deposition occurs in the interstitial space. The fibrin is subsequently replaced by collagen fibers. The increase in interstitial fibrosis may lead to parenchymal atrophy, which initiates a second phase of increased vascular permeability again resulting in the deposition of collagen in place of parenchymal cells. Most of the information supporting this hypothesis has been obtained in histological studies. Indeed, in many tissues oedema and fibrin deposition have been observed before late fibrosis [4, 6, 26, 27]. These functional studies showed that the threshold for these endpoints is between 10 and 20 Gy (delivered by a single irradiation) in animal tissues. These values are likely comparable with the total doses to the normal tissues in current clinical RT schedules, which are usually >20 Gy, even if they are usually delivered in multiple daily fractions. A proof of this behaviour can also be found in the investigation of tissue response to radiation using diagnostic imaging [28]. We have included the effect of oedema formation in the model by a perturbation of the reference value for interstitial pressure in nearby tissues (i.e. far field pressure): slightly negative values (subatmospheric nature) in the untreated condition [25], and the reference value for the oedema condition.

The temporal progression of the insult during treatment As a physical agent, the fractionated RT has the peculiar characteristic of affecting the microvasculature by irradiation constantly repeated in time (24 hours gap between one session and the following one, with an exception for the weekend). As discussed by Denham and colleagues "many of the inflammatory phenomena that evolve in response to each radiation fraction does not dissipate within 24 h, thus leading to an accumulating response". In other words the IR insult acts every day on a more and more inflamed tissue [1]. The "fractionated inflammatory insult" will evolve in time, describing step by step a worsening of the capillary bed. Furthermore, this evolving process could be daily-dose depending on fractionation. The tissue worsening after two consecutive fractions of a conventional schedule (2 Gy/fr) or of a moderate hypo-fractionated scheme (>2 Gy/fr) could have a different effect. In addition, the scheduling effect is more pronounced if we consider the last week of treatment, which are characterized by higher damage on a higher inflamed system.

This complex aspect of temporal progression of IR damage has been preliminary introduced in the model by testing the vascular network with different initial conditions (i.e. by step variation of the initial network parameters for those physical quantities that are affected by the IR insult). The choice of these

altered parameters is reflecting a long time elapsed from the beginning of the RT or a high dose per fraction, or even a mix of both situations. Therefore, our current description is related to different level of impairment of the system. Future experimental and clinical measurements are already planned within the project in which this work is included (AIRC IG 21479), and they will provide a link between the cause-effect relationship between dose, tissue damaging and also the developing time of such phenomena.

2.4 Geometrical and modelling settings

The study design includes a geometrical representation of vessels as the one shown in Figure 3. The network has an inlet and outlet channel and describes the fluid dynamics of four connected hexagons. This is a first graphical representation of a capillary bed which allows the study of the effect of RT perturbations. We have started from this simple geometry in order to easily understand the variations of the parameters affected by RT, which were never studied within this computational model. The network is built in such a way that (i) meta-arterioles are placed in the left side of the first vertical line shown in Figure 3 (nominal radius in the range between 7.20 and 10.0 μm, thickness between 0.13 and 0.20 μm); in between the two vertical lines we have the placement of the capillaries (nominal radius in the range between 4.5 and 6.5 μm, thickness between 0.03 and 0.06 μm); while post-capillary venules are on the right side (nominal radius in the range between 9.00 and 16 μm, thickness between 0.10 and 0.20 μm). The model discriminates between the three functional units in the untreated settings according to:

- the local blood pressure values, with meta-arterioles in the range of 28-22 mmHg, capillaries are between 22-18 mmHg and post-capillary venules between 18-12 mmHg;
- the shape of the vessels, particularly using the thickness-to-radius ratio; this value higher than 0.15 the blood vessel is a meta-arteriole, otherwise venules and capillaries, which differ by the radius (larger than 7 μm post-capillary venule, on the contrary a capillary).

We here recall that these values of the vessel geometry are defined in the undeformed condition, i.e., before that the blood flow enters into the network. Radii will increase by this effect reaching range of values that are more consistent for the capillary bed (10-20 μm for the meta-arterioles, 5-10 μm for the capillaries and 10-25 μm for the post-capillary venules.

Even if the computational model is already able to define proper functional characteristic for each vessel of the network, as a first step, only geometrical and pressure criteria have been considered as discriminative factors between the three units of the capillary bed. All the other parameters do not differ between vessels, and therefore they are considered as an average value between the whole geometrical structure. Moreover, since we modelled a microvascular volume of 0.02 mm^3, we have done the approximation of uniform dose within

the domain. Finally, to ensure a correct velocity in the network, we imposed increasing surfaces at every y-shape bifurcation or confluence, as expected by the continuity equation. This was done respecting the dimensional range of each functional unit.

2.5 Variations in the blood-tissue exchange

In the first test, we have varied four parameters of the model simultaneously:

1. the inlet blood pressure (p_{in}) to describe the acute vasodilation;
2. the hydraulic conductivity and the osmotic reflection coefficient to show the effects of the increased membrane permeability (L_p and σ, respectively);
3. the increased interstitial reference pressure (p_0) to include the impaired fluid extravasation.

We model three well-separated scenarios of the radiation-damage response. In the first, we describe a network with p_{in}, L_p, σ and p_0 in the nominal "physiological" range to have an overview of the healthy patients, which consists in the condition before the RT ("baseline scenario"). The third scenario represents a capillary bed embedded in a tissue with oedema and fibrin deposition ("oedema scenario"). The second scenario is in between the first and the third, representing a moderate level of impairment of both network and interstitial space ("intermediate scenario").

2.6 Variation in the vessel wall elasticity

The second analysis has been performed to test the effects of perturbations on the elasticity modulus of the vascular wall. We started from the general settings of the "oedema scenario" and we applied a variation of the Young's Modulus E. Basically, this perturbation is caused by structural changes in the constituents of the vessel wall. A functional reason of this variation can be attributed to the needed of an increased blood supply in the capillary bed of the inflamed tissue.

3 Results

In these simulations, we defined a network included in a geometrical domain of 0.36 x 0.36 x 0.18 mm^3, to be able to take into account the fluid re-absorption due to the lymphatic drainage. The domain has been scaled to be consistent with the superficial capillary density of 100 capillaries per mm^2. We then considered a thickness of 0.18 mm in order to describe the 3D characteristics of the model.

Possible range of values for the model parameters was derived from a literature search. Particularly, we started from the values of Table 1, in which we separated between parameters: (a) non-affected by RT, (b) affected by RT and (c) depending/subordinated to the variation of the affected parameters. In the

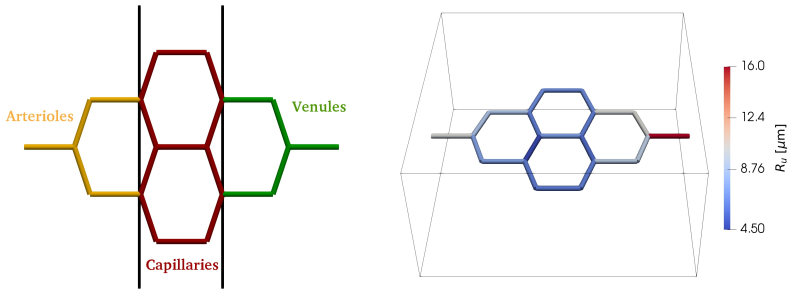

Figure 3: *Schematic representation of the geometry used in the simulations. The scheme on the left is the map of the functional units involved in the network, while the radii plotted in the image on the right represents the nominal values R_u that were given to the model as input. Dimensions of the vessels differed in every study according to the condition of the other parameters that affect the fluid transport.*

Table 1: *Values of the relevant input parameters of the model and their relationship with the ionizing radiation effect and the acute inflammatory response. In the section of the changed variables, each parameter is characterised by three different values, representing the input value for the baseline, the intermediate and the oedema scenario respectively.*

Symbol	Parameter	Unit	Value	Explanation
		Changed Variables		
p_{in}	Blood Pressure at the inlet	mmHg	28 - 30 - 32	From a nominal value for a capillary network to increased values to describe the vasodilation of the acute inflammation
p_0	Far field pressure	mmHg	-2 - 1.5 - 5	From the negative nominal values to the standard number under the presence of Oedema
L_p	Wall Hydraulic Conductivity	$m^2\ s\ kg^{-1}$	0.5 - 1 - 5 $\cdot 10^{-12}$	To describe the increasing permeability for both the mechanism
σ	Osmotic Reflection Coefficient	[-]	0.9 - 0.85 - 0.80	of transudation and exudation
E	Elastic Modulus	MPa	9.9 - 6.6 - 3.3 $\cdot 10^{-2}$	Due to the beginning process of ECs swelling, infiltration of substances, cell death and for the increasing permeability
		Dependent Variables		
R_u	Average radius within the vessel in the undeformed configuration	μm	from 5.5 to 16 for the smallest capillary and the largest venule	The input values are then deformed in every scenario according to the functional parameters of the network (permeability, local and external pressure, wall elasticity)
		Unchanged Variables		
H	Hematocrit at the inlet	[-]	0.40	Nominal values between 0.40 and 0.45. It varies within the network due to fluid leakage while red blood cells cannot cross the membrane
ν	Blood Viscosity at the inlet	$kg\ m^{-1}\ s^{-1}$	2.5 $\cdot 10^{-3}$	It varies within the network and is affected by the hematocrit
h_u	Vessel Thickness in the undeformed configuration	μm	from 0.3 to 2 for the most thin capillary and the most thick arteriole	Unchanged in the acute phase. To be considered for intermediate phase effects
p_{out}	Blood Pressure at the outlet	mmHg	12	Inflammation affects the inlet value. Pressure into and at the end of the capillary bed are usually guaranteed by the vascular resistance of the arteriole and or by the pre-capillary sphincter
$\Delta\pi$	Oncotic gradient	mmHg	(26-8)=18	Due to the progressive unbalanced fluid exchange this delta could be affected by the inflammatory response in future studies

latter we included the radii of the vessels. Indeed, the nominal radii (shown in Figure 3) were preserved through the different scenarii but the effective measure of the cross-sections varied on the basis of the following factors: (a) the local blood pressure (mainly dependent from the value p_{in} imposed at the inlet), (b) the wall elasticity, (c) the interstitial pressure p_t. For what concerns the unvaried parameters, presumably, they can be modified by the inflammatory response following the ionizing irradiation, but we currently consider this alteration of secondary relevance.

3.1 The baseline

In this setting, we defined the network of the "healthy" patient (no cardiovascular diseases, no comorbidities related to the cardiovascular system, no substance abuse and no obesity) before the beginning of the RT. This was our "reference level". The baseline values for p_{in}, p_0, L_p and σ are shown in Table 1 (section "Value", left column).

3.2 Oedema formation

We want to investigate the progressive damage to the network due to IR. Compared to the baseline, we altered the first four model parameters of Table 1: the blood pressure at the inlet p_{in} (increased from 28-32 mmHg), the far field pressure p_0 (from -2 to 5 mmHg which is the standard value for "oedema"), the wall hydraulic conductivity L_p (from $0.5 \cdot 10^{-12}$ to $5 \cdot 10^{-12}$ $m^2 s K g^{-1}$) and finally the osmotic reflection coefficient σ (from 0.90 to 0.80). We derived an intermediate level of network impairment and, then, a scenario where oedema occurred in the interstitial space. Figure 4 shows pressures (top) and velocities (bottom) characterizing the network and the interstitial volume in three different possible scenarii (one scenario for each column). A sort of "time flow" is depicted from left to right: (1) the first column as a state before the beginning of RT, (2) the second column, a state in the middle of the whole treatment and (3) the third column, last week of RT or acute phase after RT completion. Figure 4 could also be seen as the description of the acute phase after RT completion for microvasculature in different geographical settings: (1) far from the dose field, (2) close or into an organ at risk and (3) into the Planning Target Volume. For a direct quantitative comparison of variables among the different scenarii we used a single metric scale. This choice limits the possibility to observe the local changes for the different variables that the model can describe. For instance, if we consider the pressure p_t in the intermediate scenario, the fluid exchange is a trigger for variation of the interstitial pressure from 1.19 mmHg on the right of the network (venule reabsorption) to 2.7 mmHg on the left side (extravasation through the arteriolar wall), being 1.5 mmHg the nominal value p_0 (far field value). This unbalance in the fluid kinetic (toward the external flow) is driven by the increased blood pressure at the inlet (from 28 mmHg to 30 mmHg in the intermediate state) which shifts the region of the equilibrium point between hydrostatic and oncotic pressure toward the post-capillary venules giving less

surface for the interstitial fluid to get back in the capillary ends. However, this cannot be evinced directly from the plot in Figure 4. We refer to Figure 5 for a better visualization. Thus, the simulations were consistent with the description of an oedema formation, in which the leakage of fluid is not balanced from the lymphatic drainage and from the reabsorption of waste substances at the end of capillaries or in the venule y-shaped bifurcation. As a consequence fluid persists in the interstitial space and increases the local hydrostatic pressure. In addition, even under the alteration of the network caused by the acute inflammatory response, the system was still able to ensure a decreasing velocity from left to right which is important in promoting the exchange of nutrients between the microcirculation and the surrounding organ or tissue.

3.3 Vessel wall elasticity

This test is based on the settings of the third column of Figure 4, i.e. the "oedema scenario". We acted on the system by a variation of the blood wall elasticity, i.e. by the change of the Young's modulus E. It was scaled from 9.9 to 3.3 $\cdot 10^{-2} MPa$. The first scenario described an unaltered value of E compared to the baseline. In the second and third settings we started to include in the system the effects of the endothelial layer impairment, of the sloughing of the ECs and also the replacement of the capillary lumen by collagen, together with the requirements of an higher blood volume in the network and of a biophysical "tool" to reduce the increased blood velocity caused by an increasing pressure at the inlet. This scenario progressively evolves in the acute phase becoming evident in the intermediate phase (weeks to months after RT end) where it is added the effect of the first capillary occlusions which induce a fluid rearrangement and overload of some vessels.

Figure 6 shows: in the first row, the radius deformations in the network with the increase of the vessel wall elasticity; in the second row, the variation of the two components of the blood velocity as a function of E. In these configurations no occlusions were obtained as outputs of the network. On the contrary, with the decrease of the endothelial stiffness, the vessels are able to collect a greater blood volume. With respect to the functional units we can see how post-capillary venules, which have the lower thickness-to-radius ratio, are the more deformable channels. However, this deformation has an impact on the correct decreasing trend of the blood velocity from left to right, which is not preserved with the decreasing of the Young's Modulus. Particularly in the last configuration with E=$3.3 \times 10^{-2} Mpa$ where some capillaries show a velocity u_v comparable with the one of the meta-arterioles. As already discussed, in real word, this stress does not allow the right exchange of gas and nutrients with the environment. Finally, looking at the u_t in the three scenarii, we need to highlight that, even if the variations at the left side of the domain (external flow) are more pronounced, a consistent increased is expressed also on the right side (internal flow) where the post-capillary venules are more prone to collect the fluid.

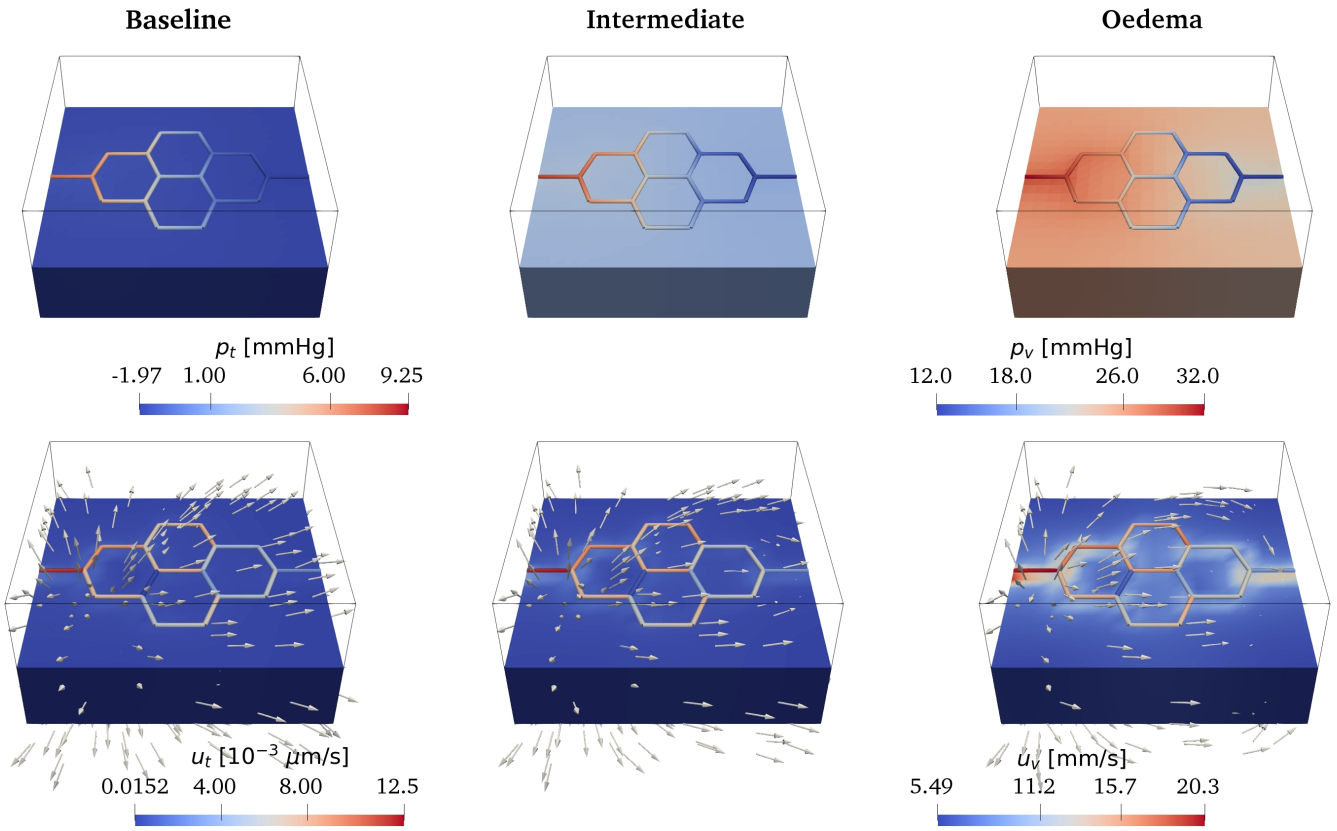

Figure 4: *Fluid dynamics variables: pressures $p_t[mmHg]$ and $p_v[mmHg]$ (top) and velocities $\boldsymbol{u}_t[\mu m/s]$ and $u_v[mm/s]$ (bottom) for the baseline (left), intermediate (center) and oedema (right) states.*

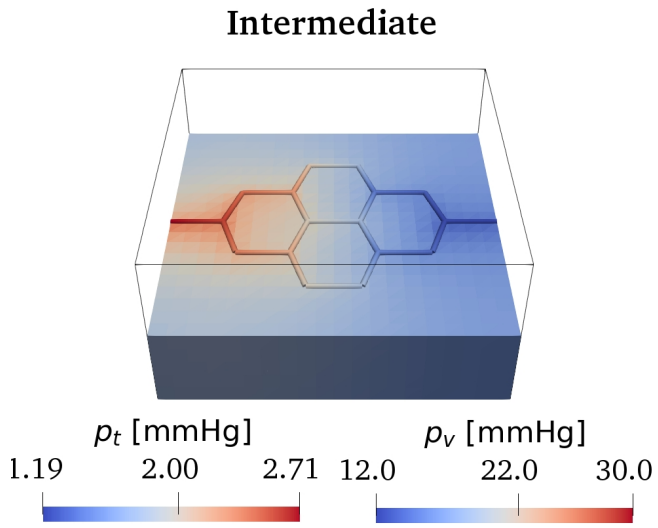

Figure 5: *Pressure $p_t[mmHg]$ in the interstitium and $p_v[mmHg]$ in the vascular network for the intermediate state.*

4 Discussion

In this work we have developed a computational model for microcirculation in compliant vessels with the ability to describe the perturbation on the network due to the presence of an acute inflammatory response. The investigated stress factor which activated the response of the immune system is the ionizing radiation delivered by radiotherapy. The first proof that radiation seriously affects the vascular system was found 4 years after the discovery of the X-rays [1] when vascular sceloris was recognised as a characteristic feature of late radiation injury. Nevertheless, the biological pathways leading to chronic dysfunctions or even to macrovascular diseases after RT has its origin in the acute phase of the inflammatory response. The dose-damage to small structures of the capillary bed can trigger an irreversible and progressive process as the one described in our model.

Two of the main features of this acute process, which have been included as input in the computational model, are the vasodilation and the variation of the endothelial permeability with the consequent increase in the fluid exchange and the deposition of fibrin or the formation of oedema. These conditions can induce fibrosis or impairment of the interstitial space over time. In parallel, alterations within the cell and the cell matrix of the endothelium can induce the occlusions of the finest capillaries or promote the formation of thrombi which block the larger capillaries. The consequent reduction in the capillary density leads to region of hypoxia and necrosis or lacking of nutrients in the healthy tissues.

The results of this work shows a first step toward the challenging aim to

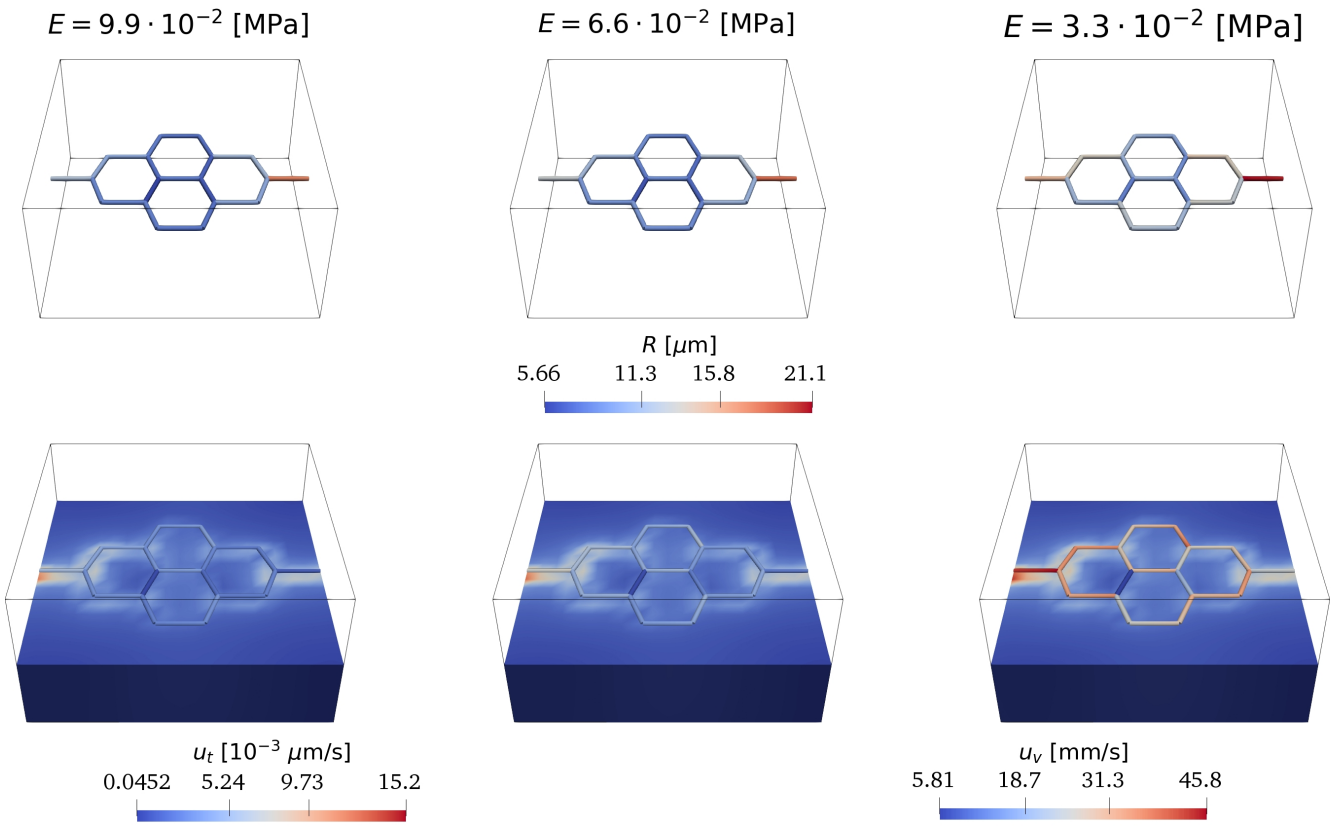

Figure 6: *Influence of the Young modulus E: the variations of the radii R characterizing the branches of the network (top) and the velocities $\mathbf{u}_t[\mu m/s]$ and $u_v[mm/s]$(bottom) for different values of E ($9.9 \cdot 10^{-2}$[MPa] left, $6.6 \cdot 10^{-2}$[MPa] center, $3.3 \cdot 10^{-2}$[MPa] right).*

describe the effect of IR on the microvasculature by means of a mechanistic modelling. Particularly, the model is able to describe the unbalance in the physical features which progressively leads to the accumulation of fibrin and oedema in the interstitial space. The second set of simulations has been able to model an impaired environment in which the variations in the vessel wall elasticity are enough to impact on the distribution of the blood flow velocity.

These preliminary results will be strengthened by a tuning of the model parameters which will be performed with the implementation of a set of features for each vessel of the network. In this way, the computational model will consider the intra-network variations of functional parameters, whereas in this phase we approximated the parameters derived from literature by averaging on the whole capillary bed. Such a refinement in the discrimination between arterioles, capillaries and venules will make the simulation more robust and will move toward a more quantitative description.

Finally, an essential characterization of the problem will be also performed: (a) through in vitro experiments, by a set of radiobiological and functional measurements of a perfusable 3D microvascular networks on chips irradiated with different doses, including both conventional fractionation at 2 Gy/fraction and moderate/extreme hypofractionation) and (b) through in vivo evaluation, using sublingual video microscopy during the follow-up of head and neck cancer patients, thus allowing measurements of the microvascular density, of the microvascular red cell content and of the flow velocity as a function of radiotherapy dose.

This comprehensive effort will allow us to integrate the model with the causality ascribable to the RT.

5 Conclusion

The damaging process of ionizing radiations on microvasculature has a strong impact on the late toxicity to the organs at risk. The modelling approach can not neglect the effects of an impaired vascular network on the fluid exchange with the interstitial space, leading to gas, nutrients and drug release deficiencies. We here proposed the first development of a computational mechanistic model able to describe effects of impairment of the endothelial membrane and to the wall elasticity. Different scenarii were considered, starting from a healthy normal situation and then shifting to a flawed scenario, possibly describing a patient with comorbidities or a patient having already experienced several fractions of radiotherapy. The accurate prediction of the fundamental processes guiding radioinduced damage of vessels, and of their effect on the tumour microenvironment and on the release of molecules, could constitute a central step for the definition of effective trials combining different modalities (e.g. radiotherapy and chemotherapy/immunotherapy involving release of drugs), avoiding many ineffective schemes to be proved in several costly clinical trials

6 Aknowledgements

The study was supported by the grant IG 21479 of the Italian Association for Cancer Research, AIRC.

References

[1] Denham, J. and Jensen, M.H. "Resistance to blood flow in microvessels in vivo". In: *Radiother Oncol* 63.2 (May 1971), pp. 129–145. DOI: 10.1016/s0167-8140(02)00060-9.

[2] Kallman, P., Agren, A., and Brahme, E. "Tumour and Normal Tissue Responses to Fractionated Non-uniform Dose Delivery". In: *International Journal of Radiation Biology* 62.2 (1992).

[3] Dimitrievich, G., Fischer Dzoga, K., and Griem, M. L. "Radiosensitivity of vascular tissue". In: *Radiation Research* 99 (1984), pp. 511–535.

[4] Law, M. P. "Radiation-Induced Vascular Injury and Its Relation to Late Effects in Normal Tissues". In: *Advance in radiation biology* 9.2 (1981), pp. 37–73. DOI: 10.1016/B978-0-12-035409-2.50007-2.

[5] Hirst, D. G., Denekamp, J., and Travis, E. L. "Radiosensitivity of vascular tissue". In: *Radiation Research* 77 (Feb. 1979), pp. 259–275.

[6] Fajardo, L. and Stewart, J.R. "Capillary injury preceding radiation-induced myocardial fibrosis". In: *Radiology* 101 (Nov. 1971), pp. 429–433. DOI: 10.1148/101.2.429.

[7] Heemsbergen, W. and Witte, M. *The Importance of the Quality of Data. In: C Fiorino and T Rancati (Eds), Modelling Radiotherapy Side Effects*. Taylor and Frencis Group, 2019, pp. 1–21.

[8] Rancati, T., Fiorino, C., Fellin, G., Vavassori, V., Cagna, E., and Casanova Borca, V. et al. "Inclusion of clinical risk factors into NTCP modelling of late rectal toxicity after high dose radiotherapy for prostate cancer". In: *Radiotherapy and Oncology* 100 (2011), pp. 124–130.

[9] Palorini, F., Rancati, T., Cozzarini, C., Improta, I., Carillo, V., Avuzzi, B., et al. "Multi-variable models of large International Prostate Symptom Score worsening at the end of therapy in prostate cancer radiotherapy". In: *Radiotherapy and Oncology* 118 (2016), pp. 92–98.

[10] Palorini, F., Cozzarini, C., Gianolini, S., Botti, A., Carillo, V., Iotti, C., et al. "First application of a pixel-wise analysis on bladder dose-surface maps in prostate cancer radiotherapy". In: *Radiotherapy and Oncology* 119 (2016), pp. 123–128.

[11] Cicchetti, A., Rancati, T., Ebert, M., Fiorino, C., Palorini, F., and al, et. "Modelling late stool frequency and rectal pain after radical radiotherapy in prostate cancer patients: Results from a large pooled population". In: *Physica Medica* 32 (2016), pp. 1690–1697. DOI: 10.1016/j.ejmp.2016.09.018.

[12] Darby, S.C., Cutter, D.J., Boerma, M., Constine, L.S., Fajardo, L.F., and Kodama, K. et al. "Radiation-related heart disease: current knowledge and future prospects". In: *Int J Radiat Oncol Biol Phys* 76 (Mar. 2010), pp. 656–665. DOI: 10.1016/j.ijrobp.2009.09.064..

[13] Andratschke, N., Maurer, J., Molls, M., and Trott, K.R. "Late radiation-induced heart disease after radiotherapy. Clinical importance, radiobiological mechanisms and strategies of prevention." In: *Int J Radiat Oncol Biol Phys* 100 (2011), pp. 160–166. DOI: 10.1016/j.radonc.2010.08.010.

[14] Schultz-Hector, S. and Trott, K.R. "Radiation-induced cardiovascular diseases: is the epidemiologic evidence compatible with the radiobiologic data?" In: *Int J Radiat Oncol Biol Phys* 101 (Aug. 2007), pp. 10–18. DOI: 10.1148/101.2.429.

[15] Possenti, L., Di Gregorio, S., Gerosa, F. M., Raimondi, G., Casagrande, G., Costantino, M. L., et al. "A computational model for microcirculation including Fahraeus-Lindqvist effect, plasma skimming and fluid exchange with the tissue interstitium". In: *International Journal for Numerical Methods in Biomedical Engineering* 35.3 (2019). e3165 cnm.3165, e3165. DOI: 10.1002/cnm.3165.

[16] Köppl, T., Vidotto, E., Wohlmuth, B., and Zunino, P. "Mathematical modeling, analysis and numerical approximation of second-order elliptic problems with inclusions". In: *Mathematical Models and Methods in Applied Sciences* 28.05 (2018), pp. 953–978. DOI: 10.1142/S0218202518500252.

[17] Laurino, F. and Zunino, P. "Derivation and analysis of coupled PDEs on manifolds with high dimensionality gap arising from topological model reduction". In: *ESAIM: Mathematical Modelling and Numerical Analysis (ESAIM: M2AN)* (2019).

[18] Popel, A. S. and Johnson, P. C. "Microcirculation and hemorheology". In: *Annual Review of Fluid Mechanics* 37.1 (2005), pp. 43–69. DOI: 10.1146/annurev.fluid.37.042604.133933.

[19] Cattaneo, L. and Zunino, P. "Computational models for fluid exchange between microcirculation and tissue interstitium". In: *Netw. Heterog. Media* 9.1 (2014), pp. 135–159. ISSN: 1556-1801. DOI: 10.3934/nhm.2014.9.135.

[20] Causin, P. and Malgaroli, F. "Mathematical modeling of local perfusion in large distensible microvascular networks". In: *Computer Methods in Applied Mechanics and Engineering* 323 (2016).

[21] Tadjbakhsh, I. and Odeh, F. "Equilibrium states of elastic rings". In: *Journal of Mathematical Analysis and Applications* 18.1 (1967), pp. 59–74. ISSN: 0022-247X. DOI: https://doi.org/10.1016/0022-247X(67)90182-5.

[22] Celsus, A.C. "De Medicina". In: *Nicolaus (Laurentii)* (1478).

[23] Eassa, E.H. and Casarett, G.W. "Effect of epsilon-amino-n-caproic acid (EACA) on radiation-induced increase in capillary permeability." In: *Radiology* 30 (Mar. 2017), pp. 679–688. DOI: 10.1148/106.3.679.

[24] Kabacik, S. and Raj, K. "Ionising radiation increases permeability of endothelium through ADAM10-mediated cleavage of VE-cadherin". In: *Oncotarget* 30 (Sept. 2017), pp. 82049–82063. DOI: 10.18632/oncotarget.18282.

[25] Levick, J.R.and and Michel, C.C. "Microvascular fluid exchange and the revised Starling principle." In: *Cardiovasc Res.* 87 (July 2010), pp. 198–210. DOI: 10.1093/cvr/cvq062.

[26] Jennings, F.L. and Arden, A. "Development of experimental radiation pneumonitis". In: *Arch Pathol* 30 (1961), pp. 437–446.

[27] Rubin, P. and Casarett, G.W. "Clinical radiation pathology as applied to curative radiotherapy". In: *Cancer.* 22 (1968), pp. 767–778.

[28] Scalco, E., Rancati, T., Pirovano, I., Mastropietro, A., Palorini, F., and Cicchetti, A. et al. "Texture analysis of T1-w and T2-w MR images allows a quantitative evaluation of radiation-induced changes of internal obturator muscles after radiotherapy for prostate cancer." In: *Med Phys.* 45 (Apr. 2018), pp. 1518–1528. DOI: 10.1002/mp.12798.

[29] Pries, A.R., Secomb, T. W., Gessner, T., Sperandio, M. B., Gross, J. F., and Gaehtgens, P. "Resistance to blood flow in microvessels in vivo". In: *Circulation Research* 75.5 (Nov. 1994), pp. 904–915. DOI: 10.1161/01.RES.75.5.904.

[30] Pries, A. R. and Secomb, T. W. "Microvascular blood viscosity in vivo and the endothelial surface layer." In: *American journal of physiology. Heart and circulatory physiology* 289.6 (2005), H2657–H2664. ISSN: 0363-6135. DOI: 10.1152/ajpheart.00297.2005.

7 Supplementary material

7.1 A mathematical model for microcirculation

We give in the following more details about the mathematical model intoduced in Section 2 of the manuscript.

Governing equations. Equation (6) is complemented by the following formula to model the blood apparent viscosity

$$\frac{\mu}{\mu_{ref}} = \left[1 + \left(\frac{\mu_{0.45}}{\mu_{ref}} - 1\right) \frac{(1-H)^C - 1}{(1-0.45)^C - 1} \left(\frac{D}{D-1.1}\right)^2\right] \left(\frac{D}{D-1.1}\right)^2,$$

where $D = 2R_h$, being R_h the hydraulic radius, C is a phenomenologically derived coefficient obtained in [29] and $\mu_{ref} = 1.8\mu_w(37^\circ)$ is a reference viscosity, with $\mu_w(37^\circ)$ the viscosity of water at 37 Celsius. At each junction of the network, we identify how the haematocrit splits between the two daughter vessels (labelled with the indices α, β) given the flow rate and the corresponding haematocrit at the parent vessel (denoted with f). Given the blood flow

rates $Q_* = |\Sigma_*| u_{v,*}$ with $* = f, \alpha, \beta$ and the outflow hematocrit H_f, we aim to determine H_α and H_β, which provide hematocrit values at the inflow of the bifurcation branches. Using the approach of [30] we define,

$$F_{QB\alpha} = \frac{Q_\alpha}{Q_f} \quad F_{QE\alpha} = \frac{Q_\alpha H_\alpha}{Q_f H_f},$$

and we calculate these fractions by means of the following model

$$\begin{cases} F_{QE\alpha} = 0 & if\ F_{QB\alpha} \leqslant X_0 \\ \text{logit}(F_{QE\alpha}) = A + B\text{logit}(\frac{F_{QB\alpha} - X_0}{1-2X_0}) & if\ X_0 < F_{QB\alpha} < 1 - X_0 \\ F_{QE\alpha} = 1 & if\ F_{QB\alpha} \geqslant 1 - X_0 \end{cases}$$

where A, B are fixed parameters determined in [29], $\text{logit}(x) = \ln[x/(1-x)]$ and X_0 is the fractional blood flow rate under which any RBC will flow into the daughter branch α. Finally, the desired hematocrit levels are determined as

$$H_\alpha = F_{QE\alpha} H_f Q_f / Q_\alpha\,, \quad H_\beta = (1 - F_{QE\alpha}) H_f Q_f / Q_\beta\,.$$

7.2 A mathematical model for deformable microvessels

Pre-buckling regime The deformed radius of the vessel is computed as follows

$$R = R_u \left(1 + \frac{(1-\nu)}{E} B_1 - \frac{1+\nu}{E} \frac{B_2}{R_u^2}\right) \qquad \text{thick-walled ring}$$

$$R = R_u \left(1 - \frac{1-\nu^2}{\gamma E} \Delta p\right) \qquad \text{thin-walled ring}$$

where for thick vessels R denotes the internal radius and B_1, B_2 are given by

$$B_1 = \frac{p_v R_u^2 - \bar{\bar{p}}_t R_{u,e}^2}{R_{u,e}^2 - R_u^2}, \qquad B_2 = \frac{R_u^2 R_{u,e}^2 (\bar{\bar{p}}_t - p_v)}{R_{u,e}^2 - R_u^2},$$

being $R_{u,e} = R_u + h_u$ and $\bar{\bar{p}}$ is the averaged value of p_t computed on the cross section Σ.

MOX Technical Reports, last issues

Dipartimento di Matematica
Politecnico di Milano, Via Bonardi 9 - 20133 Milano (Italy)

46/2019 Di Iorio, J.; Vantini, S.
funBI: a Biclustering Algorithm for Functional Data

47/2019 Spreafico, M.; Ieva, F.
Dynamic monitoring of the effects of adherence to medication on survival in Heart Failure patients: a joint modelling approach exploiting time-varying covariates

48/2019 Di Gregorio, S.; Fedele, M.; Pontone, G.; Corno, A.F.; Zunino, P.; Vergara, C.; Quarteroni, A.
A multiscale computational model of myocardial perfusion in the human heart

44/2019 Formaggia, L.; Gatti, F.; Zonca, S.
An XFEM/DG approach for fluid-structure interaction problems with contact

45/2019 Regazzoni, F.; Dedè, L.; Quarteroni, A.
Active force generation in cardiac muscle cells: mathematical modeling and numerical simulation of the actin-myosin interaction

43/2019 Antonietti, P.F.; Mazzieri, I.; Migliorini, F.
A space-time discontinuous Galerkin method for the elastic wave equation

42/2019 Martino, A.; Guatteri, G.; Paganoni, A.M.
hmmhdd Package: Hidden Markov Model for High Dimensional Data

41/2019 Abbà, A.; Bonaventura, L.; Recanati, A.; Tugnoli, M.;
Dynamical p-adaptivity for LES of compressible flows in a high order DG framework

40/2019 Lovato, I.; Pini, A.; Stamm, A.; Vantini, S.
Model-free two-sample test for network-valued data

38/2019 Massi, M.C.; Ieva, F.; Gasperoni, F.; Paganoni, A.M.
Minority Class Feature Selection through Semi-Supervised Deep Sparse Autoencoders